GLIO: Tightly-Coupled GNSS/LiDAR/IMU Integration for Continuous and Drift-Free State Estimation of Intelligent Vehicles in Urban Areas

Xikun Liu , Weisong Wen , *Member, IEEE*, and Li-Ta Hsu , *Senior Member, IEEE*

Abstract—Intelligent vehicles demand reliable, continuous, and accurate positioning capability. Light Detection and Ranging (LiDAR)-inertial odometry (LIO) provides precise continuous relative pose estimation but suffers from drift over large-scale operations. Global navigation satellite system (GNSS) offers drift-free absolute positioning capability but the accuracy is strongly affected by non-line-of-sight (NLOS) receptions and multipath effects arising from the reflections of the surrounding environments. The tightly-coupled integration of the GNSS and LIO is highly complementary. However, how to fully utilize the complementariness of LiDAR measurements and the GNSS model is still an open question. More importantly, an open-sourced implementation of their integration is highly expected. To fill these gaps, this article proposes the GLIO, a GNSS/LiDAR/IMU integrated estimator that tightly fuses GNSS pseudorange, Doppler, LiDAR, and IMU measurements using factor graph optimization (FGO). In particular, the corrections from the reference station are adopted to remove the systematic errors involved in the GNSS pseudorange measurements. To fully exploit the complementariness of the LiDAR and GNSS measurements, two stages of the optimization scheme are utilized to achieve global consistent and continuous pose estimation. In the first stage of optimization, the sliding-window-based FGO is employed to integrate the GNSS-related factors, IMU pre-integration factor, and *scan-to-map-based* LiDAR factor for efficient odometry estimation. In the second stage of optimization, the LiDAR factor is employed as a *scan-to-multiscan* scheme to maintain global consistency and improve the robustness of the system to the GNSS outlier by large-scale batch optimization. We evaluate the proposed method and verify its effectiveness through the challenge dataset *UrbanNav* involving highly urbanized areas. The proposed system achieves more than 70% improvement in positioning accuracy compared with the traditional GNSS positioning method and LIO standalone system.

Index Terms—Global navigation satellite system (GNSS), LiDAR, sensor fusion, non-line-of-sight (NLOS), LiDAR inertial odometry, urban areas.

Xikun Liu and Weisong Wen are with Hong Kong Polytechnic University Shenzhen Research Institute, China, and also with Hong Kong Polytechnic University, Hong Kong (e-mail: xi-kun.liu@connect.polyu.hk; welson.wen@polyu.edu.hk).

Li-Ta Hsu is with Hong Kong Polytechnic University, Hong Kong (e-mail: lt.hsu@polyu.edu.hk).

I. INTRODUCTION

WITH the fast development of intelligent vehicles (IV) [1], the ability of continuous and accurate positioning in various outdoor scenarios has become a fundamental requirement [2], [3]. However, the complex and changing urban environments without prior information pose a substantial challenge for the current positioning approaches.

GNSS positioning is challenged in urban areas: Global Navigation Satellite Systems (GNSS) has long been a key technology for vehicle positioning providing unbiased global positioning solutions worldwide with an accuracy within the range of meters using low-cost receiver [4]. Through the incorporation of reference station corrections, the positioning accuracy at the scale of centimeters can be further attained. Unfortunately, GNSS positioning can be affected by the atmosphere or the environment in which the receiver is operating. Despite the double-differential (DD) combination [5] of signals from the reference station, the underlying urban environment, such as buildings [6], trees, and dynamic objects [7], can introduce large positioning errors into the system due to the non-line-of-sight (NLOS) receptions and multipath effects arising from object reflections [8].

Integration of GNSS and LIO is promising: Light detection and ranging (LiDAR) sensors provide high-accuracy, large-scale 3D point cloud information. Due to its reliability and accuracy, an increasing number of intelligent vehicles are equipped with LiDAR for positioning via LiDAR odometry [9], [10], [11] or map-based LiDAR localization [12], [13]. Benefiting from the enhancements of the inertial measurement unit (IMU) and its pre-integration methods [14], [15], the LiDAR/inertial odometry (LIO) system [16], [17] stands out as a representative solution with impressive local accuracy and robustness, especially for the GNSS-denied areas [18]. However, a large number of dynamic objects and repetitive features in city scenes can potentially degrade the performance of the LIO system [19]. In addition, its local incremental estimation will inevitably lead to drift over time [20], [21]. Theoretically, the fusion of two complementary types of information – *the global unbiased GNSS positioning*

and the local accurate LiDAR/inertial odometry–allows for a global continuous high-accuracy positioning capability. Numerous studies have investigated this combination and demonstrated its effectiveness.

A. Related Works

Loosely-coupled and tightly-coupled GNSS/LIO integration: First, depending on the level of fused information, these studies focused either a loosely-coupled manner based on the position-level information or a tightly-coupled manner based on the raw measurements from sensors. The loosely-coupled methods process the observations from GNSS and LiDAR/inertial systems separately and then fuse the estimated poses from the different systems according to their weights and uncertainties [16], [22], [23], [24], [25], [26], [27], [28]. Considering that the direct fusion of noisy GNSS positioning results may introduce errors in the system, some methods proposed to evaluate GNSS solution before integration to eliminate the impact of the unhealthy GNSS solutions: [26] performed GNSS degradation checks (e.g., through Zero-Velocity update, satellite number monitor, dilution of the precision monitor) to drop unhealthy GNSS solutions to improve the overall positioning performance. Similarly, [27] proposed to apply GNSS solution selection by comparing them with the predicted position, where the position prediction relies on a prior map. [28] proposed a scene optimizer to assess and select the solutions of GNSS for further integration. Excluding the unhealthy GNSS solutions prevents introducing gross errors to the loosely-coupled integration. However, simply discarding the GNSS solutions also prevents the system from taking advantage of healthy GNSS observations, especially in urban environments where there is a frequent shortage of satellites. Different from loosely-coupled methods, the tightly-coupled methods estimate the state directly based on raw measurements from all sensors, which enables separate mitigation of unhealthy GNSS measurements while maintaining healthy GNSS constraints [29], [30], [31]. The tightly-coupled system can benefit from the absolute constraints of GNSS even in highly urbanized areas with limited received satellite number. More importantly, the tightly-coupled integration scheme can effectively exploit the complementariness of GNSS and LiDAR measurements. The existing state-of-the-art methods rely on accurate outlier exclusion by performing residual check [29] or traditional statistical methods [30], [31], which requests a good initial guess and more healthy GNSS observations in a single epoch. Nevertheless, the biased GNSS measurements by environmental reflection can dominate the observation in a single epoch and they are not effectively detectable by traditional methods. In other words, tightly-coupled methods outperform loosely-coupled methods in terms of both data utilization and the potential to improve positioning accuracy. Still, it remains to be explored how to further utilize the information from different sensors while improving robustness to GNSS unhealthy observations in a tightly-coupled GNSS/LiDAR/IMU framework.

Filter-based and optimization-based GNSS/LIO integration: In terms of fusion methods, the studies of GNSS/LiDAR/IMU integration systems can also be categorized into two streams,

the filter-based methods and the optimization-based methods. The Kalman filter (KF) and its variants are adopted by many approaches [26], [29], [30], [31] to achieve efficient state estimation. However, the KF-based methods mainly utilize information from the two consecutive epochs for estimation and fail to revisit or optimize the past states. On the contrary, optimization-based methods use batch data, which better exploits the temporal and special correlations. Specifically, [32], [33] sufficiently demonstrate the ability of factor graph [34] to exploit information redundancy at the raw measurement level for resisting local minimal using GNSS or GNSS/IMU measurements. Research in [22], [23], [27], [28], [35] subsequently shows the improved performance and global consistency of optimization-based GNSS/LiDAR/IMU integration. Nevertheless, the above-mentioned methods use a loosely-coupled scheme for GNSS factors, which limits the potential of sensor fusion. Recently, [36] proposed to tightly fuse GNSS raw measurements with the LIO system through factor graph optimization. In this work, the factor graph consists of pseudorange factors to provide absolute positioning constraints, inter-epoch double-difference carrier-phase factors to provide relative positioning constraints, and relative pose constraints provided by IMU and LiDAR. However, the LiDAR measurement is used in a loosely coupled manner which is based on relative pose rather than raw measurements. Moreover, the Doppler measurements are not involved in the system.

B. Limitations of the Existing Works

Lack of the tightly-coupled full suit integration of the GNSS and LIO using factor graph optimization (FGO): Preliminary attempts discussed above have shown that the optimization-based tightly-coupled GNSS/LiDAR/IMU integration has the opportunity to make full use of the raw measurements while taking full account of the temporal and spatial correlations between the data, to obtain optimal state estimates. However, the tightly-coupled full suit integration of the GNSS measurements (both the Doppler and the pseudorange measurements) and LIO using the state-of-the-art FGO is not available. Moreover, an open-sourced implementation of such integration is highly expected to fill this interdisciplinary gap to further facilitate this research.

Lack of exploitation of the LiDAR measurement model in resisting the GNSS outliers: As mentioned above, the GNSS measurements are significantly degraded in urban canyons. The existing methods mainly focused on the state prediction-based residual check [29] or empirical-orientated quality assessment [26] to evaluate the GNSS measurements, which is not guaranteed in challenging environments. Moreover, the most state-of-the-art GNSS/LiDAR/IMU integrated solutions use a scan-to-map [16] scheme for LiDAR registration. It should be noted that such LiDAR constraints scheme plays a role as an absolute constraint. In the case that the trajectory has a large drift, the LiDAR factor is natural with drift error. This approach does not provide a consistent estimate for each sensor, rather leads to inconsistency between LiDAR and GNSS measurements. *In this paper, we focus on the question of whether it is possible*

to utilize both advantages of the scan-to-scan and scan-to-map based model to achieve globally consistent and locally smooth state estimation.

C. Key Contributions of This article

To address the listed two limitations above, this article proposes an optimization-based tightly-coupled GNSS/LiDAR/IMU integration system for accurate and robust positioning in complex environments. Specifically, the contributions in this article are listed as:

1) *Raw measurements level GNSS/LiDAR/IMU tightly-coupled integration with FGO:* A tightly-coupled integration scheme fusing GNSS pseudorange, Doppler measurements, LiDAR measurements, and IMU measurements through factor graph optimization.
2) *Robust and globally consistent state estimation:* A two-stage optimization-based estimator is proposed to improve robustness to unhealthy GNSS measurements and maintain the global consistency of the estimation.
3) *Open-sourced code and extensive experimentation in challenging scenarios:* The proposed method demonstrated the effectiveness through experimentation in various challenging urban scenarios in Hong Kong. To contribute to the community, the implementation of the proposed method is also open-sourced.[1]

To the best of our knowledge, this is the first attempt to integrate GNSS, LiDAR, and IMU all at raw measurement levels based on factor graph optimization together with open-sourced implementation. This article is structured as follows: Section II provides relevant definitions and notations. Section III outlines the proposed integration methods, including the detailed measurement models and residual formulations. In Section IV, the experimental design and evaluation results of the proposed method are presented. Finally, Section V offers concluding remarks and identifies potential avenues for further research and development.

II. NOTATIONS AND DEFINITIONS

A. Frame Definitions

In this article, multiple sensors and data fusion are involved. Therefore, the information of corresponding coordinate systems is firstly introduced below:

1) Earth-centered, earth-fixed (ECEF) frame: The ECEF frame $(\cdot)^{EC}$ is a three-dimensional Cartesian coordinate system that is geocentric and rotates with the Earth. It is a common reference frame used in navigation, geodesy, and satellite positioning systems as it provides a fixed reference frame that is centered on the Earth, which allows for accurate and consistent measurements of position, velocity, and acceleration.
2) East, north, and up (ENU) frame: For consistency and ease of comparison, this article utilizes the ENU frame $(\cdot)^{EN}$ as the default coordinate system for all relevant states. In the ENU frame, the X-axis points towards the East, the Y-axis

points towards the North, and the Z-axis points upwards, perpendicular to the XY plane. This frame is often used to represent the position and orientation of a point or object on the Earth's surface relative to a local reference point and serves as an intermediary between the local frame and the global frame.
3) Sensor frame: The sensor frame refers to the coordinate system that is fixed to the local sensors. Specifically, the sensor-related frames are denoted as $(\cdot)^r$, $(\cdot)^l$, and $(\cdot)^b$ for the GNSS receiver, LiDAR, and IMU frames, respectively.

B. Notations

In this article, the matrices are represented by uppercase bold letters, while the vectors are denoted by lowercase bold letters. The variables and frame coordinates are represented by italicized letters and lowercase letters denote constant scalars. We list others as:

1) The satellite's pseudorange observation is represented by the notation $\rho_{r,t}^s$, where r corresponds to the GNSS receiver, t denotes the time index, and s signifies the satellite's index;
2) The satellite's Doppler observation is denoted as $d_{r,t}^s$;
3) The satellite's position and velocity are respectively represented by $\mathbf{p}_{s,t}^{EC}$ and $\mathbf{v}_{s,t}^{EC}$;
4) The receiver's position and velocity are respectively represented by $\mathbf{p}_{r,t}^{EN}$ and $\mathbf{v}_{r,t}^{EN}$;
5) The receiver clock bias for specific satellite constellation system i is denoted as $\delta_{r,t}^i$, while the receiver clock bias drift is represented by $\dot{\delta}_{r,t}^i$. The satellite clock bias is represented by $\delta_{s,t}$, and the satellite clock bias drift is denoted by $\dot{\delta}_{s,t}$. It should be noted that the receiver clock bias drift is shared across multiple satellite systems;
6) The reference station's position is denoted by $\mathbf{p}_e^{EC}$. Its corresponding pseudorange observation is represented by $\rho_{e,t}^s$;
7) The origin reference point to define the ENU frame is $\mathbf{p}_o^{EC}$;
8) The frame transformation is given by $\mathbf{T}_A^B = [\mathbf{R}_A^B \ \mathbf{p}_A^B]$, where A denotes the source frame and B denotes the target frame. The rotation is represented by $\mathbf{R}_A^B$ with quaternion form as $\mathbf{q}_A^B$. The translation is denoted by $\mathbf{p}_A^B$.

III. METHODOLOGY

A. System Overview

The workflow of the proposed system is illustrated in Fig. 1, It comprises four main steps, which are the data preprocessing, the factor formulation, the sliding-window-based first stage optimization, and the batch-optimization-based second stage fusion. The system's inputs consist of GNSS measurements (including raw pseudorange and Doppler measurements), LiDAR measurements, and IMU measurements. To manage computational load, the proposed system utilizes a keyframe mode for processing measurements. The pre-integration method [14] is implemented to convert raw IMU measurements into relative constraints and propagate the initial pose of keyframes.

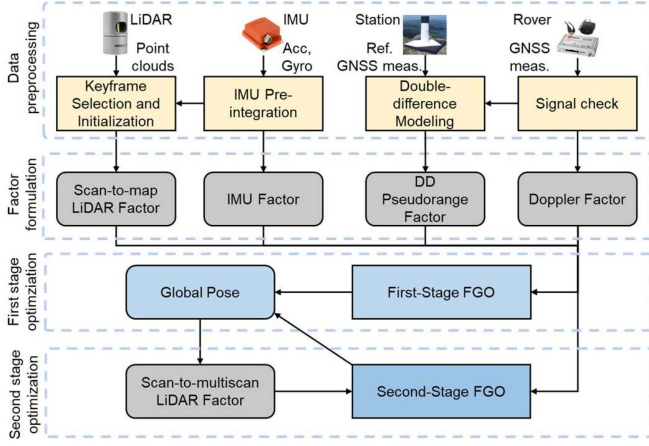[1][Online].Available: https://github.com/XikunLiu-huskit/GLIO

Fig. 1. Overview of the system pipeline.

Subsequently, a first stage sliding-window-based factor graph is formulated, which includes a double-differenced (DD) pseudorange factor, Doppler factor, scan-to-map LiDAR factor, and IMU pre-integration factor. Once the preprocessing is completed, the states are optimized using factor graph optimization (FGO) in a joint manner. Moreover, the second stage batch optimization is performed at a certain time interval. For batch fusion, a large factor graph is maintained with similar GNSS and IMU constraints. Notably, the LiDAR factor is formulated as a scan-to-multiscan scheme to avoid local minimum and maintain global consistency.

The states are maintained of the IMU-centric body frame in the ENU coordinate. The following are the states in detail:

a) The kth keyframe's pose states, including the position $\mathbf{p}_{b,k}^{EN}$ and orientation $\mathbf{q}_{b,k}^{EN}$.

b) The kth keyframe's velocity $\mathbf{v}_{b,k}^{EN}$. Additionally, $\mathbf{b}_a$ denotes the bias of the accelerometer and $\mathbf{b}_w$ represents the bias of the gyroscope.

c) The receiver clock drift $\dot{\delta}_{r,t}$.

The states can be further expressed as:

$$\boldsymbol{\chi} = \left[x_0, \cdots, x_k, \dot{\delta}_{t_0}^r, \cdots, \dot{\delta}_{t_{n-1}}^r \right]$$

$$\text{With } x_k = \left[\mathbf{p}_{b,k}^{EN}, \ \mathbf{q}_{b,k}^{EN}, \ \mathbf{v}_{b,k}^{EN}, \ \mathbf{b}_a, \ \mathbf{b}_w \right] \quad (1)$$

where $t \in [t_0, \cdots, t_{n-1}]$ denotes the GNSS epoch, while n denotes the received GNSS total epochs within the sliding window.

The optimal state estimation is determined by maximizing the posterior probability of the given measurements. Assuming that the measurements are uncorrelated and the corresponding noise follows a zero-mean Gaussian-distribution, we demonstrate the problem in the following form to illustrate the constraints involved and the corresponding weighting strategy:

$$\boldsymbol{\chi}^* = \mathrm{argmin}_{\boldsymbol{\chi}} \sum_{S,r,k,t} (\|\mathbf{r}_p - \mathbf{H}_p \boldsymbol{\chi}\| + \|\mathbf{r}_{L,k}\|_{\boldsymbol{\Sigma}_L}^2 + \|\mathbf{r}_{B,k}\|_{\boldsymbol{\Sigma}_B}^2$$

$$+ \|\mathbf{r}_{DD,\rho,r,t}^S\|_{\sigma_\rho}^2 + \|\mathbf{r}_{d,r,t}^S\|_{\sigma_d}^2) \quad (2)$$

where the marginalized term as prior constraints is denoted by $\{\mathbf{r}_p, \mathbf{H}_p\}$. The IMU factor is represented by $\mathbf{r}_{B,k}$ and weighted

by the covariance matrix $\boldsymbol{\Sigma}_B$. Similarly, the LiDAR factor is represented by $\mathbf{r}_{L,k}$ and weighted by its relative covariance matrix $\boldsymbol{\Sigma}_L$. The GNSS pseudorange and Doppler factors are denoted by $\mathbf{r}_{DD,\rho,r,t}^S$ and $\mathbf{r}_{d,r,t}^S$, respectively. The corresponding uncertainty of Doppler measurements is specifically set to ten times smaller than pseudorange measurements as $10 * \sigma_d = \sigma_\rho$, where the initial calculation of σ_ρ is based on the SNR and elevation angle [37].

B. Factor Formulation

In this section, the observation modeling and the factor formulation of the sensors are introduced, including DD pseudorange factor, the Doppler factor, the LiDAR factor, and the IMU pre-integration factor.

1) GNSS DD Pseudorange Factor: The pseudorange observation function is given by:

$$\rho_{r,t}^s = r_{r,t}^s + c\left(\delta_{r,t} - \delta_{s,t}\right) + I_{r,t}^s + T_{r,t}^s + \varepsilon_{\rho,\ r,t}^s \quad (3)$$

where $\rho_{r,t}^s$ denotes the received pseudorange measurement by receiver r from satellite s at epoch t. The real geometric range is given by $r_{r,t}^s$. The ionospheric delay and the tropospheric delay are represented by $I_{r,t}^s$ and $T_{r,t}^s$, respectively. The rest errors, including the error arising from NLOS or multipath receptions, receiver, and antenna-related noise errors are represented by $\varepsilon_{\rho,\ r,t}^s$.

To prevent the system from introducing gross errors caused by clock synchronization problems or the atmosphere delay, we adopt the DD technique by performing single-difference twice between receivers (user receiver r and reference station e) and between satellites (satellite s and master satellite w). The satellite with the highest elevation angle in the corresponding epoch is selected as the master satellite, which is less prone to multipath and NLOS receptions. The DD pseudorange measurement is given by:

$$\rho_{DD,r,t}^s = \left(\rho_{r,t}^s - \rho_{e,t}^s\right) - \left(\rho_{r,t}^w - \rho_{e,t}^w\right) \quad (4)$$

With other error sources being eliminated, the DD pseudorange prediction model can be further derived as:

$$\rho_{DD,r,t}^s = \left(r_{r,t}^s - r_{e,t}^s\right) - \left(r_{r,t}^w - r_{e,t}^w\right) + \varepsilon_{DD,\rho,r,t}^s \quad (5)$$

where $\varepsilon_{DD,\rho,r,t}^s$ represents the noise error term and the residual is given as:

$$r_{DD,\rho,r,t}^s = \rho_{DD,r,t}^s - \left(r_{r,t}^s - r_{e,t}^s\right) - \left(r_{r,t}^w - r_{e,t}^w\right) \quad (6)$$

where the range distances $r_{r,t}^s$, $r_{e,t}^s$, $r_{r,t}^w$ and $r_{e,t}^w$ are the distance from receiver r and base station e to satellite s and w at epoch t, which are calculated based on their ECEF positions. As the states are maintained in the ENU frame, to calculate the residual, we convert the receiver position at epoch t in the ENU frame $\mathbf{p}_{r,t}^{EN}$ to ECEF frame $\mathbf{p}_{r,t}^{EC}$ through the following equations:

$$\mathbf{p}_{r,t}^{EC} = \mathbf{R}_{EN}^{EC} \mathbf{p}_{r,t}^{EN} + \mathbf{p}_o^{EC} \quad (7)$$

$$\mathbf{R}_{EN}^{EC} = \begin{bmatrix} -sin\lambda_o & -sin\phi_o cos\lambda_o & cos\phi_o cos\lambda_o \\ cos\lambda_o & -sin\phi_o sin\lambda_o & cos\phi_o sin\lambda_o \\ 0 & cos\phi_o & sin\phi_o \end{bmatrix} \quad (8)$$

where the ECEF origin point is denoted as $\mathbf{p}_o^{EC}$, which can be obtained through various initialization methods, such as trajectory alignment between locally generated trajectory (e.g., by LIO) and globally generated trajectory (e.g., by GNSS). The geographic longitude ϕ_o and geographic latitude λ_o are directly calculated from the ECEF origin point $\mathbf{p}_o^{EC}$.

The lever-arm transformation from an IMU-centered position $\mathbf{p}_{b,t}^{EN}$ to receiver position $\mathbf{p}_{r,t}^{EN}$ is obtained through extrinsic parameters:

$$\mathbf{p}_{r,t}^{EN} = \mathbf{p}_{b,t}^{EN} + \mathbf{R}_{r,t}^{EN}\mathbf{p}_r^b \tag{9}$$

where $\mathbf{p}_r^b$ is lever-arm translation.

Notably, the timestamp of the LiDAR keyframe t_k is different from GNSS epoch time t. In this article, we use the interpolation method to align GNSS measurements to LiDAR timestamps. Given the LiDAR keyframe-related states $\mathbf{p}_{b,k}^{EN}$ and $\mathbf{p}_{b,k+1}^{EN}$ in the adjacent moment t_k and t_{k+1} with $t \in [t_k, t_{k+1}]$, the GNSS epoch-related state $\mathbf{p}_{b,t}^{EN}$ can be calculated as:

$$\mathbf{p}_{b,t}^{EN} = \left\{ \frac{t - t_k}{t_{k+1} - t_k}\mathbf{p}_{b,k}^{EN} + \frac{t_{k+1} - t}{t_{k+1} - t_k}\mathbf{p}_{b,k+1}^{EN} \right\} \tag{10}$$

2) GNSS Doppler Factor: The Doppler observation function is given by:

$$\lambda d_{r,t}^s = \mathbf{e}_{r,t}^{s,LOS}\left(\mathbf{v}_{s,t}^{EC} - \mathbf{v}_{r,t}^{EC}\right) + \mathrm{c}\left(\dot{\delta}_{r,t}^i - \dot{\delta}_{s,t}\right) + \varsigma_{r,t}^s \tag{11}$$

where $\varsigma_{r,t}^s$ denotes the noisy error term, c represents the speed of light, while λ is the carrier wavelength of the signal. The receiver velocity in the ECEF frame is obtained from the states in the ENU frame by $\mathbf{v}_{r,t}^{EC} = \mathbf{R}_{EN}^{EC}\mathbf{v}_{r,t}^{EN}$. $\mathbf{e}_{r,t}^{s,LOS}$ is the line-of-sight unit vector, which points the satellite from the receiver calculated by:

$$\mathbf{e}_{r,t}^{s,LOS} = \left(\frac{\mathbf{p}_{s,t}^{EC} - \mathbf{p}_{r,t}^{EC}}{||\mathbf{p}_{s,t}^{EC} - \mathbf{p}_{r,t}^{EC}||}\right)^T \tag{12}$$

Therefore, the residual of Doppler measurement is given by:

$$r_{d,r,t}^s = d_{r,t}^s - \frac{1}{\lambda_i}\left(\mathbf{e}_{r,t}^{s,LOS}\left(\mathbf{v}_{s,t}^{EC} - \mathbf{v}_{r,t}^{EC}\right) + \mathrm{c}\left(\dot{\delta}_{r,t}^i - \dot{\delta}_{s,t}\right)\right) \tag{13}$$

3) Inertial Factor: The inertial sensor provides acceleration and angular velocity observations, which are affected by bias and additive noises. In comparison to other perception and positioning sensors like LiDAR and GNSS, its higher measurement frequency leads to the development of pre-integration method and wide utilization of the corresponding method for efficient sensor fusion [14]. The method pre-integrates multiple raw measurements to establish a relative pose constraint from keyframe k to its next adjacent keyframe $k + 1$. The implementation of IMU pre-integration follows [38], the relevant theories are omitted here and interested readers can refer to [14], [38] for more information in detail.

4) LiDAR Factor of Scan-to-Map Model: In this work, Li-DAR measurements are similarly utilized as the mainstream feature-based LiDAR SLAM methods [17], [39]. The so-called scan-to-map scheme data association for the LiDAR factor is depicted in Fig. 2. By evaluating the performance that separately
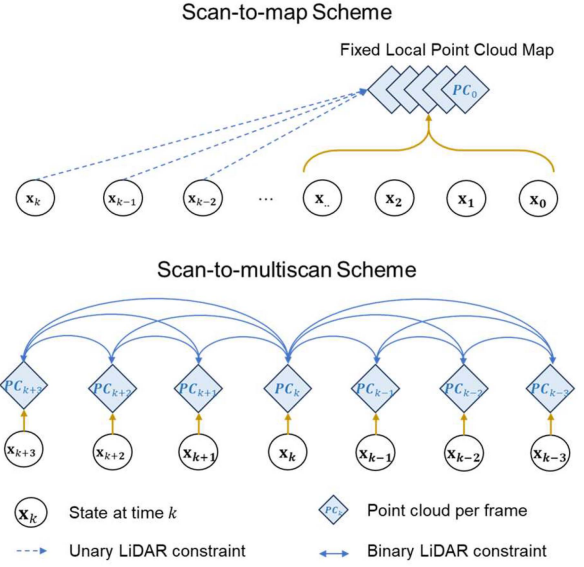

Fig. 2. Illustration of the scan-to-map vs scan-to-multi-scan association for LiDAR factor formulation.

using edge-feature and plane-feature for LiDAR odometry, it is observed that the planar features provide a performance with better robustness and higher accuracy. Therefore, planar points are utilized in the implementation and the edge points are not involved. To select planar feature points, we extract local patches from the point cloud of the keyframe to evaluate their local distribution, the points satisfying the planar distribution are selected. Then, to identify plane correspondences, the nearest-neighbor search method is adopted between the source point clouds and the target point cloud, which are from keyframes and local map. Finally, the point-to-plane scan-to-map residual is computed based on the feature point $\mathbf{p}_{p,k}^{EN}$ in keyframe k, and the corresponding feature points $\mathbf{p}_{p,k,a}^{EN,M}$, $\mathbf{p}_{p,k,b}^{EN,M}$ and $\mathbf{p}_{p,k,c}^{EN,M}$, representing the planar patch in the local point cloud map M [39]:

$$r_{l,s,k}^{s-mp} = \frac{\left\| \begin{pmatrix} \left(\mathbf{p}_{p,k}^{EN} - \mathbf{p}_{p,k,a}^{EN,M}\right) \\ \left(\mathbf{p}_{p,k,a}^{EN,M} - \mathbf{p}_{p,k,b}^{EN,M}\right) \times \left(\mathbf{p}_{p,k,a}^{EN,M} - \mathbf{p}_{p,k,c}^{EN,M}\right) \end{pmatrix} \right\|}{\left\| \left(\mathbf{p}_{p,k,a}^{EN,M} - \mathbf{p}_{p,k,b}^{EN,M}\right) \times \left(\mathbf{p}_{p,k,a}^{EN,M} - \mathbf{p}_{p,k,c}^{EN,M}\right) \right\|} \tag{14}$$

$$\mathbf{p}_{p,k}^{EN} = \mathbf{R}_{b,k}^{EN}\left(\mathbf{R}_l^b\mathbf{p}_{p,k}^l + \mathbf{p}_l^b\right) + \mathbf{p}_{b,k}^{EN} \tag{15}$$

where the planar point in the local sensor frame is represented by $\mathbf{p}_{p,k}^l$, it is transformed from the LiDAR frame to the IMU frame through $\mathbf{T}_l^b = [\mathbf{R}_l^b \; \mathbf{p}_l^b]$. Then it is further transformed from the body frame to the ENU frame by $\mathbf{T}_{b,k}^{EN} = [\mathbf{R}_{b,k}^{EN} \; \mathbf{p}_{b,k}^{EN}]$.

5) LiDAR Factor of Scan-to-Multiscan Model: As we have discussed above, since the local point cloud map is fixed, the scan-to-map-based LiDAR constraint essentially can be regarded as an absolute constraint without global positioning information. This approach is problematic for large-scale integration as drift-free alignment between local coordinate and
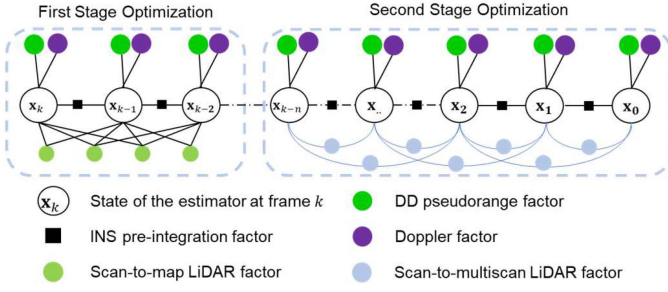
Fig. 3. Illustration of the factor graph structure of the proposed first stage fusion and second stage optimization.

global coordinate cannot be guaranteed. To address this issue, we proposed to use scan-to-multiscan LiDAR factor for tight integration to maintain global consistency with absolute constraints from GNSS, which is illustrated in Fig. 2: For each keyframe k, the adjacent m keyframes are associated to provide high-accuracy scan-to-scan planar constraints, where the same plane residual formulation model is adopted and the pose states of both corresponding target and source keyframes are involved. In detail, the residual of the scan-to-multiscan LiDAR planar factor is formed as:

$$r_{l,s,k}^{s-ms} = \frac{\left\| \begin{pmatrix} \mathbf{p}_{p,k}^{EN} - \mathbf{p}_{p,k+i,a}^{EN} \end{pmatrix} \\ \begin{pmatrix} \mathbf{p}_{p,k+i,a}^{EN} - \mathbf{p}_{p,k+i,b}^{EN} \end{pmatrix} \times \begin{pmatrix} \mathbf{p}_{p,k+i,a}^{EN} - \mathbf{p}_{p,k+i,c}^{EN} \end{pmatrix} \right\|}{\left\| \begin{pmatrix} \mathbf{p}_{p,k+i,a}^{EN} - \mathbf{p}_{p,k+i,b}^{EN} \end{pmatrix} \times \begin{pmatrix} \mathbf{p}_{p,k+i,a}^{EN} - \mathbf{p}_{p,k+i,c}^{EN} \end{pmatrix} \right\|}$$
(16)

$$\mathbf{p}_{p,k}^{EN} = \mathbf{R}_{b,k}^{EN} \left(\mathbf{R}_l^b \mathbf{p}_{p,k}^l + \mathbf{p}_l^b \right) + \mathbf{p}_{b,k}^{EN}$$
(17)

$$\mathbf{p}_{p,k+i,abc}^{EN} = \mathbf{R}_{b,k+i}^{EN} \left(\mathbf{R}_l^b \mathbf{p}_{p,k+i,abc}^l + \mathbf{p}_l^b \right) + \mathbf{p}_{b,k+i,abc}^{EN}$$
$$\text{where } i \in [-m, m]$$
(18)

The proposed scan-to-multiscan LiDAR factor brings two advantages. On the one hand, it provides relative constraints only, which enables consistent integration between global GNSS and local LiDAR. On the other hand, the scan-to-multiscan association between multiple keyframes enhances the relative pose information and thus increases the weight during optimization, which contributes to a smoother local trajectory and better robustness to outliers from other sensors.

6) Marginalization Factor: To reduce computational complexity while retaining the impact of previous information constraints, we adopt marginalization in the sliding-window-based optimization process in the first stage fusion. This involves gradually marginalizing constraints from previous keyframes using the Schur complement method [40]. After marginalizing the constraints from older keyframes, a new prior factor is added to the updated window.

C. Factor Graph Construction on the First Stage and the Second Stage Fusion

The factor graph of the two stages of optimization is shown in Fig. 3, where the marginalization factor of the sliding-window-based first stage fusion is omitted. The main difference between the first and the second stage lies in the formulation of the LiDAR factor. For the first stage, the factor graph is formulated in a short sliding window to provide an efficient estimation. Within the short time window, the GNSS measurements are limited and prone to outliers. Differently, the LiDAR measurements can maintain high accuracy over a short period. Therefore, the LiDAR factor is employed based on a scan-to-map scheme, where the local map is built through previous keyframe states as high-quality prior information. In this way, the GNSS measurements can assist LIO for reliable position and velocity estimation in highly dynamic environments. To ensure a balanced impact of GNSS, LiDAR, and IMU during optimization, we limit the number of LiDAR features to 100 for each keyframe by random selection, and the LiDAR residuals are dynamically weighted based on the covariance information considering the number ratio between LiDAR and GNSS measurements [41].

On the other side, we follow our previous work in [42] and proposed to fuse the GNSS factor, the IMU factor, with the scan-to-multiscan LiDAR factor for the second stage optimization. Specifically, each LiDAR keyframe is associated with 12 adjacent keyframes, for each frame pair, only 25 planar features are randomly selected to decrease the computational load and balance the weight between different factors. Moreover, the batch optimization in the second stage is iterated 3 times for residual-based outlier detection and exclusion [42]. It is very important that the factor graph in the second stage is able to greatly enhance the constraint redundancy for the states while maintaining global consistency, enabling accurate outlier detection and exclusion. In short, the second stage batch optimization is able to use a sufficient number of healthy GNSS measurements over a long period, and together with the strong relative pose constraints from LiDAR and IMU, finally achieves the globally consistent and locally robust optimization. The second stage fusion is performed in another thread and updates the global states once finishing the optimization.

IV. EXPERIMENTAL RESULTS

In this work, we implement the proposed system through C++ on Robot Operation System (ROS) [43]. Ceres Solver [44] is utilized to solve the nonlinear optimization problem. To evaluate the performance, we conduct experiments on challenging sequences from the *UrbanNav* dataset [45]. The sequences can represent typical urban canyons, which pose significant challenges to GNSS receptions due to densely distributed tall blockages.

In the first evaluated sequence, denoted as *TST*, the vehicle started underneath an overpass and passed through a commercial area densely occupied by tall office buildings, and the road was always accompanied by heavy traffic. The overall narrowness of the roadway limits the sky visibility in most of the time. A small portion of the trajectory has a one-sided distribution of tall

buildings, which will help to mitigate the consistently unhealthy GNSS signal. For the second sequence, named *Whampoa*, the data lasts for more than 25 min and 4.5 km. Vehicle departed from the open sky area and passed through dense urban areas, involving dense buildings, small tunnels, and heavy traffic. The tunnel environments and the narrow residential roads make it difficult for GNSS to provide healthy measurements. In addition, the vehicle is often surrounded by multiple double-deckers, which severely affects both GNSS and LiDAR observations. These pose serious challenges to the positioning capability of the system.

A. Experiment Platform

The *UrbanNav* experimental platform includes multiple sensors. In this work, the u-blox F9P as a low-cost GNSS receiver is used to collect raw single-frequency GPS/Bei Dou/Galileo/GLONASS signals at a rate of 10 Hz. Inertial measurements are collected at 100 Hz using the Xsens Ti-10 IMU, and Velodyne HDL-32E collects point cloud data at 10 Hz. To provide ground truth, we utilize the NovAtel SPAN-CPT, which performs multiple frequencies and constellations GNSS Real-time kinematic (RTK) with a tactical IMU. The trajectory is further post-processed to ensure the centimeter-level accuracy. The extrinsic parameters are priorly calibrated for use.

B. Evaluation Comparison

The proposed method is evaluated by conducting a qualitative and quantitative comparison with several other representative methods based on multiple aspects. To evaluate the positioning accuracy of different methods, three aspects of error in terms of mean, maximum, and standard deviation in 2D and 3D cases are compared. The evaluated methods are listed as:

   a) *RTK:* RTKLIB [46] is first evaluated to demonstrate the performance of the conventional GNSS-RTK method. All GNSS measurements are involved, including pseudorange, carrier phase, and Doppler measurements. In detail, we use forward and backward filtering with the fix and hold mode.
   b) *LIO:* As one of the representative LIO systems as well as part of the basis for the proposed system, LILI-OM [17] is evaluated for comparison. The alignment of the local frame to the world frame is given by the ground truth.
   c) *LIO-GNSS:* As the state-of-the-art GNSS/LiDAR/IMU fusion method, LIO-SAM [16] is evaluated with differential GNSS (DGNSS) result from RTKLIB.
   d) *GLIO-SS:* The proposed tightly-coupled GNSS/LiDAR/IMU integrated system with only the single stage optimization implemented. This is to show the effectiveness of the fusion of GNSS, IMU, and scan-to-map LiDAR factors.
   e) *GLIO-DS:* The proposed tightly-coupled GNSS/LiDAR/IMU integrated system with both first and second stages optimization. This is to show the effectiveness of the integration of GNSS, IMU, and scan-to-multiscan LiDAR factors and the final performance of the proposed method.

TABLE I
EVALUATED POSITIONING ERROR OF THE FOUR METHODS IN TST

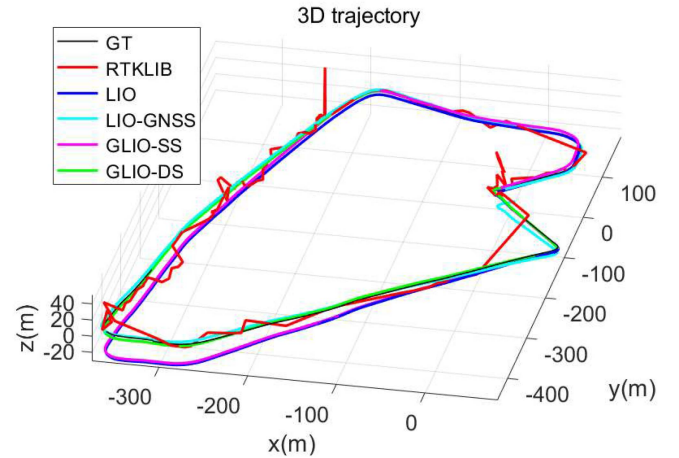| ALL DATA	RTKLIB	LIO	LIO-GNSS	GLIO-SS	GLIO-DS
2D MEAN	7.53	2.21	3.24	1.53	**1.21**
2D MAX	46.27	4.47	5.26	4.00	**2.57**
2D STD	7.76	1.19	0.61	1.11	**0.39**
3D MEAN	18.02	10.33	5.28	9.64	**2.07**
3D MAX	93.69	30.15	19.01	28.38	**4.69**
3D STD	14.70	9.35	3.01	9.10	**0.88**
FIX.	7.1%				

Fig. 4. 3D trajectory in TST. The black, red, blue, cyan, magenta, and green curves denote the trajectory of ground truth, RTKLIB, LIO, LIO-GNSS, GLIO-SS, and GLIO-DS, respectively.

1) Evaluation of Data TST: Table. I shows the evaluation results evaluated in TST, where MEAN denotes the mean positioning error in meters, MAX denotes the maximum error in meters, STD denotes the standard deviation in meters, FIX represents the fix rate of GNSS-RTK provided by RTKLIB. Figs. 4 and 5 depict the trajectory and the positioning errors. Notably, the initial state is provided by ground truth for the LIO and the GNSS-SS method for coordinate alignment. There are tens of meters of jumps in the error of the RTKLIB throughout the traveling interval. They are due to uninterrupted tall buildings, frequent overpasses, billboards, as well as interference from surrounding dynamic objects. It is observed that the RTKLIB only achieves a 7.1% fix rate, which indicates the degree of deterioration of the quality of GNSS signal in urban areas. The RTKLIB only resulted in a 2D mean error of 7.53 meters with a maximum error of 46.27 meters, and a 3D mean error of 18.02 meters with a maximum error of 93.69 meters. The LIO method achieved a 2D mean error of 2.21 meters. Due to the short length of the trajectory, the overall 2D accuracy of LIO is less affected by drift. However, the tendency of the trajectory to drift is still clearly evident.

The LIO-GNSS achieves a 2D mean error of 3.24 meters and a 3D mean error of 5.28 meters. Compared with LIO, the LIO-GNSS significantly reduces the 3D mean error through
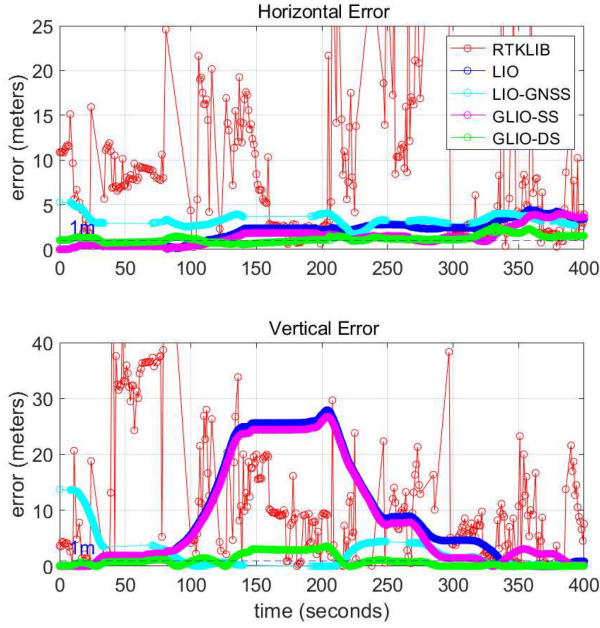
Fig. 5. Positioning error in TST. The red, blue, cyan, magenta, and green curves denote the error of RTKLIB, LIO, LIO-GNSS, GLIO-SS, and GLIO-DS, respectively.
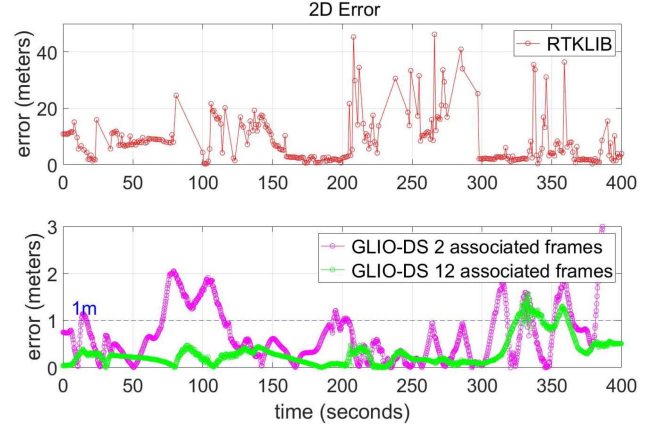

Fig. 6. 2D positioning error through RTKLIB and GLIO-DS with different multiscan pairs. The red, magenta, and green curves denote the error of RTKLIB, GLIO-DS with 2 adjacent frame pairs as well as with 12 adjacent frame pairs, respectively. Notably, the error from the lever arm in this figure is compensated by prior calibration.

loosely-coupled pose graph optimization (PGO). However, the LIO-GNSS fails to achieve consistent results in the TST sequence. The maximum error reaches 5.26 meters in 2D and 19.01 meters in 3D. Fig. 5 shows that there is a large error margin within the first 50 seconds. The reasons are for two aspects: (1) The TST sequence starts from a highly urbanized area, where the filter-based DGNSS by RTKLIB fails to obtain reliable accuracy and covariance of the estimated position, which introduces large bias to the pose graph. (2) Severe satellite occlusion over long periods prevents the correction of the current epoch by neighboring epochs. This illustrates that, for loosely-coupled systems, a long period of continuous harsh environment can seriously deteriorate the final performance. On the other side, The GLIO-SS method, which tightly fuses the raw GNSS measurements with scan-to-map LiDAR and IMU measurements, demonstrates substantial improvement over RTKLIB and standalone LIO methods. Specifically, it reduces the 2D error to 1.53 meters, while the standard deviation and maximum error are 1.11 and 4.00 meters. As mentioned above, the LIO can maintain accuracy at a pretty high level in such a short trajectory. Therefore, when the LiDAR is assigned with higher weight, the adopted scan-to-map LiDAR factor is effective in mitigating the impact of unhealthy GNSS observations for integrated system and helping to achieve better results. However, GNSS-SS fails to mitigate the vertical drift from LIO. It can be concluded that there are two drawbacks to GLIO-SS. Firstly, the weighting of the residuals from different sensors is not well balanced. During the epochs with few satellite observations, reducing the weight of the GNSS residuals prevents the system from using the GNSS information effectively, and enlarging the GNSS residuals makes the system less robust to outliers. Secondly, the lack of consistency in the construction of the optimization problem

makes the system always biased when estimating the state. These two drawbacks limit the performance of a tightly-coupled integration system. Eventually, GLIO-DS is performed to further demonstrate the effectiveness of the proposed two stages of optimization. GLIO-DS demonstrates superior performance with 2D errors of 1.21 meters, with standard deviation and maximum error of 0.39 meters and 2.57 meters, respectively. More importantly, the vertical drift is corrected substantially. It should be noted that there is no prior information for GNSS-DS, therefore, it proves that the second stage optimization effectively mitigates the impact of unhealthy GNSS observations through the construction of consistent optimization problems and batched utilization of long periods of data to achieve better performance.

a) Further exploration of scan-to-multiscan LiDAR factor: To further demonstrate the effectiveness of the scan-to-multiscan LiDAR factor, we further compared the GLIO-DS with different associated frame numbers, namely with 2 adjacent frames and 12 adjacent frames. The latter frame number is selected considering both accuracy and computational efficiency. As shown in Fig. 6, GLIO-DS with more associated frames achieves significant improvement on local smoothness and global accuracy. GLIO-DS with only 2 associated frames suffers from limitations on relative pose information. The comparison result proves that the scan-to-multiscan LiDAR factor can provide high-quality relative constraint, which is highly complementary to other absolute constraints, enabling lossless and consistent global estimation.

2) Evaluation of Data Whampoa: The evaluated positioning error of the five methods in Whampoa is shown in Table II. MEAN denotes the positioning error in meters. MAX denotes the maximum error in the trajectory. STD denotes the standard deviation. FIX represents the fix rate of GNSS-RTK provided by RTKLIB. The LIO method shows significant drift with increasing driving distance, resulting in a maximum 2D error of 45.51 meters at the end of the trajectory. The quality of GNSS measurements is also clearly shown by the low fix rate in Table II. The vehicle starts the trajectory from an open sky area, where the

TABLE II
EVALUATED POSITIONING ERROR OF THE FOUR METHODS IN WHAMPOA

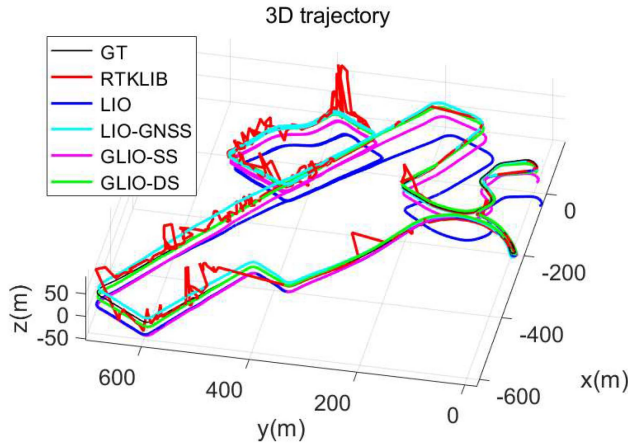| ALL DATA	RTKLIB	LIO	LIO-GNSS	GLIO-SS	GLIO-DS
2D MEAN	7.74	12.63	2.68	4.40	**1.68**
2D MAX	49.37	45.51	5.73	15.27	**4.17**
2D STD	10.11	12.55	1.44	3.80	**0.96**
3D MEAN	9.90	28.36	7.44	14.72	**3.34**
3D MAX	98.85	69.06	23.91	30.09	**9.15**
3D STD	15.67	16.94	5.84	7.76	**2.21**
FIX.	17.3%				

Fig. 7. 3D trajectory in Whampoa. The black, red, blue, cyan, magenta, and green curves denote the trajectory of ground truth, RTKLIB, LIO, LIO-GNSS, GLIO-SS, and GLIO-DS, respectively.
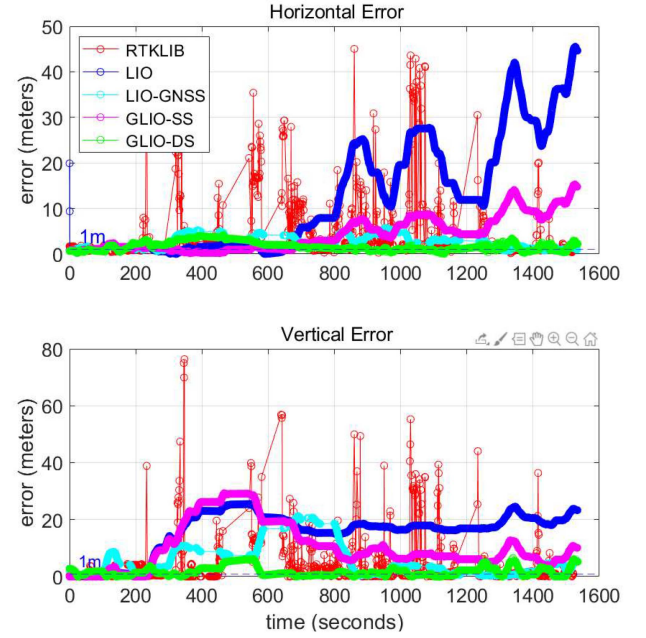

Fig. 8. Positioning error in Whampoa. The red, blue, cyan, magenta, and green curves denote the error of RTKLIB, LIO, LIO-GNSS, GLIO-SS, and GLIO-DS, respectively.

positioning result of RTKLIB is maintained within two meters. However, based on Figs. 7 and 8, in the intervals from 300 s to 350 s, from 400 s to 600 s, and around 1000 s, when the vehicle travels through sparse high-rise buildings, dense and narrow residential paths, and medium-height building environments, respectively, the GNSS positioning accuracy is severely affected by up to several tens of meters. The RTKLIB method results in a 2D mean error of 7.74 meters with a maximum error of 49.37 meters and a 3D mean error of 9.90 meters with a maximum error of 98.85 meters.

The evaluation result of the GLIO-SS method is shown in Table II by suppressing the system errors to some extent but failing to maintain local smoothness due to huge biases in GNSS measurements therefore resulting in relatively high positioning error. Specifically, it achieves a 2D error of 4.40 meters, while the standard deviation and maximum error are 3.80 and 15.27 meters. LIO-GNSS achieves reliable accuracy and robustness with a 2D mean error of 2.68 meters and a 3D mean error of 7.44 meters. However, the loosely-coupled method strongly relies on the quality of the position estimation of accuracy and uncertainty. As a result, the accuracy of LIO-GNSS fluctuates considerably in several challenging areas, especially for the vertical axis. Ultimately, GLIO-DS achieves the best performance among all the compared methods with 2D errors of 1.68 meters and standard deviation and maximum error of 0.96 meters and 4.17

meters, respectively. The GLIO-DS also achieves much better performance on vertical accuracy and obtains a 3D mean error of 3.34 with 9.15 meters as a maximum, despite the challenging environments.

In conclusion, the proposed tightly-coupled GNSS/LiDAR/ IMU integrated positioning method tightly fuses the GNSS pseudorange measurements, Doppler measurements, LiDAR measurements, and IMU measurements through a common factor graph optimization. Secondly, it mitigates the effects of GNSS outliers through globally consistent large-scale FGO at the second stage fusion, which improves positioning accuracy and robustness.

3) Analysis of Computational Efficiency: Regarding computational efficiency, the data preprocessing, the first stage fusion and the second stage optimization are the main parts for time-consuming. We adopt the open-sourced LILI-OM [17] as the LIO basis for the proposed system, therefore, the data preprocessing and frontend optimization share a similar cost of time. The preprocessing of GNSS, IMU measurements, and scan-to-map LiDAR features for the first stage and the scan-to-multiscan LiDAR features for the second stage fusion together cost less than 40 ms per frame. The first stage fusion takes around 30 ms, which is less than baseline backend fusion as fewer LiDAR constraints are selected for the optimization problem. Moreover, we set the maximum iteration number as 50 and the maximum optimization time as 3 s for the second stage optimization on a separate thread. The local pose re-initialization takes less than 10 ms. Therefore, the total time consumption for the system is less than 100 ms per frame, which enables real-time operation on 10 hz LiDAR sensors.

V. CONCLUSION

Modern intelligent vehicles demand higher continuous positioning accuracy due to their diverse outdoor application scenarios. This article presents GNSS/LiDAR/IMU tightly-coupled odometry that: (1) tightly fuses the GNSS, LiDAR, and IMU all at raw measurement level through FGO, and (2) employs two stages optimization including sliding-window based optimization and batch-based fusion to achieve efficient, consistent and robust positioning solutions. Within the proposed two stages of optimization, different LiDAR factors such as the scan-to-map scheme in the first stage and the scan-to-multiscan scheme in the second stage are employed. Experimental results on several challenging sequences collected in Hong Kong demonstrate the effectiveness of the proposed method by achieving reliable accuracy and robustness in challenging urban environments utilizing commercial-level GNSS receivers and a LiDAR/IMU sensor kit.

Importantly, this work is presented in the fusion thread in our 3D LiDAR-aided (3DLA) GNSS framework. Based on the results presented above, it is observed that the system still has a maximum error of nearly 10 meters. This is because the unhealthy GNSS observations are not fully mitigated, and the available healthy GNSS observations are insufficient to correct the trajectory. In the future, we want to further explore the fusion system in terms of raw data quality improvement and positioning methods. For the first point, we hope to use point cloud data to recover the reflection of the transmitted signals and correct the biased observations of unhealthy GNSS signals, thus radically improving the quality of the raw GNSS data and increasing positioning accuracy. Second, we want to further explore the proposed system together with our previous 3DLA GNSS real-time kinematic (RTK) positioning methods [41], [42] to investigate the possibilities of centimeter-level positioning in highly challenging urban areas for commercial-level GNSS receivers. Moreover, it is worth expanding the current implemented GNSS positioning method to the more competitive GNSS positioning approaches such as Precise Point Positioning (PPP) to simplify the system deployment and increase the range of applications.

REFERENCES

[1] L. Chen et al., "Milestones in autonomous driving and intelligent vehicles: Survey of surveys," *IEEE Trans. Intell. Veh.*, vol. 8, no. 2, pp. 1046–1056, Feb. 2023.

[2] A. Chalvatzaras, I. Pratikakis, and A. A. Amanatiadis, "A survey on map-based localization techniques for autonomous vehicles," *IEEE Trans. Intell. Veh.*, vol. 8, no. 2, pp. 1574–1596, Feb. 2023.

[3] T. G. Reid et al., "Localization requirements for autonomous vehicles," *SAE Int. J. Connected Automated Veh.*, vol. 2, no. 12-02-03-0012, pp. 173–190, 2019.

[4] E. D. Kaplan and C. Hegarty, *Understanding GPS/GNSS: Principles and Applications*. Norwood, MA, USA: Artech House, 2017.

[5] P. K. Enge, "The global positioning system: Signals, measurements, and performance," *Int. J. Wireless Inf. Netw.*, vol. 1, no. 2, pp. 83–105, 1994.

[6] W. Wen, G. Zhang, and L. T. Hsu, "Correcting NLOS by 3D LiDAR and building height to improve GNSS single point positioning," *Navigation*, vol. 66, no. 4, pp. 705–718, 2019.

[7] W. Wen, G. Zhang, and L.-T. Hsu, "GNSS NLOS exclusion based on dynamic object detection using LiDAR point cloud," *IEEE Trans. Intell. Transp. Syst.*, vol. 22, no. 2, pp. 853–862, Feb. 2021.

[8] L.-T. Hsu, "Analysis and modeling GPS NLOS effect in highly urbanized area," *GPS Solutions*, vol. 22, no. 1, 2018, Art. no. 7.

[9] T. Shan and B. Englot, "LeGO-LOAM: Lightweight and ground-optimized lidar odometry and mapping on variable terrain," in *Proc. IEEE/RSJ Int. Conf. Intell. Robots Syst.*, 2018, pp. 4758–4765.

[10] H. Guo, J. Zhu, and Y. Chen, "E-LOAM: LiDAR odometry and mapping with expanded local structural information," *IEEE Trans. Intell. Veh.*, vol. 8, no. 2, pp. 1911–1921, Feb. 2023.

[11] S. Liang, Z. Cao, C. Wang, and J. Yu, "Hierarchical estimation-based LiDAR odometry with scan-to-map matching and fixed-lag smoothing," *IEEE Trans. Intell. Veh.*, vol. 8, no. 2, pp. 1607–1623, Feb. 2023.

[12] Z. Wang, J. Fang, X. Dai, H. Zhang, and L. Vlacic, "Intelligent vehicle self-localization based on double-layer features and multilayer LIDAR," *IEEE Trans. Intell. Veh.*, vol. 5, no. 4, pp. 616–625, Dec. 2020.

[13] L. Li, M. Yang, H. Li, C. Wang, and B. Wang, "Robust localization for intelligent vehicles based on compressed road scene map in urban environments," *IEEE Trans. Intell. Veh.*, vol. 8, no. 1, pp. 250–262, Jan. 2023.

[14] C. Forster, L. Carlone, F. Dellaert, and D. Scaramuzza, "On-manifold preintegration for real-time visual–inertial odometry," *IEEE Trans. Robot.*, vol. 33, no. 1, pp. 1–21, Feb. 2017.

[15] L. Zhang, W. Wen, L.-T. Hsu, and T. Zhang, "An improved inertial preintegration model in factor graph optimization for high accuracy positioning of intelligent vehicles," *IEEE Trans. Intell. Veh.*, early access, Jun. 08, 2023, doi: 10.1109/TIV.2023.3282623.

[16] T. Shan, B. Englot, D. Meyers, W. Wang, C. Ratti, and D. Rus, "Lio-sam: Tightly-coupled lidar inertial odometry via smoothing and mapping," in *Proc. IEEE/RSJ Int. Conf. Intell. Robots Syst.*, 2020, pp. 5135–5142.

[17] K. Li, M. Li, and U. D. Hanebeck, "Towards high-performance solid-state-lidar-inertial odometry and mapping," *IEEE Robot. Automat. Lett.*, vol. 6, no. 3, pp. 5167–5174, Jul. 2021.

[18] M. Maaref, J. Khalife, and Z. M. Kassas, "Lane-level localization and mapping in GNSS-challenged environments by fusing lidar data and cellular pseudoranges," *IEEE Trans. Intell. Veh.*, vol. 4, no. 1, pp. 73–89, Mar. 2019.

[19] J. Zhang, M. Kaess, and S. Singh, "On degeneracy of optimization-based state estimation problems," in *Proc. IEEE Int. Conf. Robot. Automat.*, 2016, pp. 809–816.

[20] G. Bresson, Z. Alsayed, L. Yu, and S. Glaser, "Simultaneous localization and mapping: A survey of current trends in autonomous driving," *IEEE Trans. Intell. Veh.*, vol. 2, no. 3, pp. 194–220, Sep. 2017.

[21] W. Wen and L.-T. Hsu, "AGPC-SLAM: Absolute ground plane constrained 3D LiDAR SLAM," *NAVIGATION: J. Inst. Navigation*, vol. 69, no. 3, 2022.

[22] G. He, X. Yuan, Y. Zhuang, and H. Hu, "An integrated GNSS/LiDAR-SLAM pose estimation framework for large-scale map building in partially GNSS-denied environments," *IEEE Trans. Instrum. Meas.*, vol. 70, 2021, Art. no. 7500709.

[23] L. Chang, X. Niu, T. Liu, J. Tang, and C. Qian, "GNSS/INS/LiDAR-SLAM integrated navigation system based on graph optimization," *Remote Sens*, vol. 11, no. 9, 2019, Art. no. 1009.

[24] J. Zhang, W. Wen, F. Huang, X. Chen, and L.-T. Hsu, "Continuous GNSS-RTK aided by LiDAR/inertial odometry with intelligent GNSS selection in urban canyons," in *Proc. 34th Int. Tech. Meeting Satell. Division Inst. Navigation*, 2021, pp. 4198–4207.

[25] L. Li, M. Yang, L. Guo, C. Wang, and B. Wang, "Hierarchical neighborhood based precise localization for intelligent vehicles in urban environments," *IEEE Trans. Intell. Veh.*, vol. 1, no. 3, pp. 220–229, Sep. 2016.

[26] X. Meng, H. Wang, and B. Liu, "A robust vehicle localization approach based on GNSS/IMU/DMI/LiDAR sensor fusion for autonomous vehicles," *Sensors*, vol. 17, no. 9, 2017, Art. no. 2140.

[27] W. Wu, X. Zhong, D. Wu, B. Chen, X. Zhong, and Q. Liu, "LIO-fusion: Reinforced lidar inertial odometry by effective fusion with GNSS/relocalization and wheel odometry," *IEEE Robot. Automat. Lett.*, vol. 8, no. 3, pp. 1571–1578, Mar. 2023.

[28] H. Chen, W. Wu, S. Zhang, C. Wu, and R. Zhong, "A GNSS/LiDAR/IMU pose estimation system based on collaborative fusion of factor map and filtering," *Remote Sens*, vol. 15, no. 3, 2023, Art. no. 790.

[29] T. Li, L. Pei, Y. Xiang, X. Zuo, W. Yu, and T.-K. Truong, "P^3-LINS: Tightly coupled PPP-GNSS/INS/LiDAR navigation system with effective initialization," *IEEE Trans. Instrum. Meas.*, vol. 72, 2023, Art. no. 8501813.

[30] S. Li, S. Wang, Y. Zhou, Z. Shen, and X. Li, "Tightly coupled integration of GNSS, INS, and LiDAR for vehicle navigation in urban environments," *IEEE Internet Things J*, vol. 9, no. 24, pp. 24721–24735, Dec. 2022.

[31] X. Li, H. Wang, S. Li, S. Feng, X. Wang, and J. Liao, "GIL: A tightly coupled GNSS PPP/INS/LiDAR method for precise vehicle navigation," *Satell. Navigation*, vol. 2, pp. 1–17, 2021.

[32] W. Wen, T. Pfeifer, X. Bai, and L.-T. Hsu, "Factor graph optimization for GNSS/INS integration: A comparison with the extended Kalman filter," *NAVIGATION: J. Inst. Navigation*, vol. 68, no. 2, pp. 315–331, 2021.

[33] N. Sünderhauf, M. Obst, S. Lange, G. Wanielik, and P. Protzel, "Switchable constraints and incremental smoothing for online mitigation of non-line-of-sight and multipath effects," in *Proc. IEEE Intell. Veh. Symp.*, 2013, pp. 262–268.

[34] F. Dellaert, "Factor graphs and GTSAM: A hands-on introduction," *Georgia Inst. Technol.*, Atlanta, GA, USA, Tech. Rep. GT-RIM-CP&R-2012-002, 2012.

[35] X. He, S. Pan, W. Gao, and X. Lu, "LiDAR-inertial-GNSS fusion positioning system in urban environment: Local accurate registration and global drift-free," *Remote Sens.*, vol. 14, no. 9, 2022, Art. no. 2104.

[36] J. Beuchert, M. Camurri, and M. Fallon, "Factor graph fusion of raw GNSS sensing with IMU and lidar for precise robot localization without a base station," in *Proc. IEEE Int. Conf. Robot. Automat.*, 2023, pp. 8415–8421.

[37] A. M. Herrera, H. F. Suhandri, E. Realini, M. Reguzzoni, and M. C. de Lacy, "goGPS: Open-source MATLAB software," *GPS Solutions*, vol. 20, pp. 595–603, 2016.

[38] T. Qin, P. Li, and S. Shen, "VINS-Mono: A robust and versatile monocular visual-inertial state estimator," *IEEE Trans. Robot.*, vol. 34, no. 4, pp. 1004–1020, Aug. 2018.

[39] J. Zhang and S. Singh, "LOAM: Lidar odometry and mapping in real-time," in *Proc. Robot.: Sci. Syst.*, vol. 2, no. 9, 2014, pp. 1–9.

[40] G. Sibley, L. Matthies, and G. Sukhatme, "Sliding window filter with application to planetary landing," *J. Field Robot.*, vol. 27, no. 5, pp. 587–608, 2010.

[41] X. Liu, W. Wen, F. Huang, H. Gao, Y. Wang, and L.-T. Hsu, "3D LiDAR aided GNSS NLOS mitigation for reliable GNSS-RTK positioning in urban canyons," 2022, *arXiv:2212.05477*.

[42] X. Liu, W. Wen, and L.-T. Hsu, "3D LiDAR aided GNSS real-time kinematic positioning via coarse-to-fine batch optimization for high accuracy mapping in dense urban canyons," in *Proc. 35th Int. Tech. Meeting Satell. Division Inst. Navigation*, 2022, pp. 1954–1965.

[43] M. Quigley et al., "ROS: An open-source robot operating system," in *Proc. ICRA Workshop Open Source Softw.*, 2009, vol. 3, pp. 5.

[44] S. Agarwal and K. Mierle, "Ceres solver," 2012. [Online]. Available: http://ceres-solver.org

[45] L.-T. Hsu et al., "UrbanNav: An open-sourced multisensory dataset for benchmarking positioning algorithms designed for urban areas," in *Proc. 34th Int. Tech. Meeting Satell. Division Inst. Navigation*, 2021, pp. 226–256.

[46] T. Takasu and A. Yasuda, "Development of the low-cost RTK-GPS receiver with an open source program package RTKLIB," in *Proc. Int. Symp. GPS/GNSS*, 2009, pp. 1–6.

Weisong Wen (Member, IEEE) received the B.Eng. degree in mechanical engineering from Beijing Information Science and Technology University, Beijing, China, in 2015, the M.Eng. degree in mechanical engineering from China Agricultural University, Beijing, China, in 2017, and the Ph.D. degree in mechanical engineering from The Hong Kong Polytechnic University (PolyU), Hong Kong, in 2020. In 2018, he was also a Visiting Ph.D. student with the Faculty of Engineering, University of California, Berkeley (UC Berkeley), CA, USA. Before joining PolyU as an Assistant Professor in 2023, he has been a Research Assistant Professor with AAE of PolyU since 2021. He has authored or coauthored 30 SCI papers and 40 conference papers in the field of GNSS (ION GNSS+) and navigation for Robotic systems (IEEE ICRA, IEEE ITSC), such as autonomous driving vehicles. He was the recipient of the innovation award from TechConnect 2021, Best Presentation Award from the Institute of Navigation (ION) in 2020, and First Prize in Hong Kong Section in Qianhai-Guangdong-Macao Youth Innovation and Entrepreneurship Competition in 2019 based on his research achievements in 3D LiDAR aided GNSS positioning for robotics navigation in urban canyons. The developed 3D LiDAR-aided GNSS positioning method has been reported by top magazines such as Inside GNSS and has attracted industry recognition with remarkable knowledge transfer.

Li-Ta Hsu (Senior Member, IEEE) received the B.S. and Ph.D. degrees in aeronautics and astronautics from National Cheng Kung University, Taiwan, in 2007 and 2013, respectively. He is currently an Associate Professor with the Department of Aeronautical and Aviation Engineering, The Hong Kong Polytechnic University, Hong Kong, before he was a Postdoctoral Researcher with the Institute of Industrial Science, University of Tokyo, Tokyo, Japan. In 2012, he was a Visiting Scholar with University College London, London, U.K. His research interests include GNSS positioning in challenging environments and localization for pedestrians, autonomous driving vehicle, and unmanned aerial vehicle.

Xikun Liu received the bachelor's degree in mechanical design, manufacturing, and automation from the Huazhong University of Science and Technology, Wuhan, China, in 2017, and the master's degree in mechatronics and information technology from the Karlsruhe Institute of Technology, Karlsruhe, Germany, in 2021. He is currently working toward the Ph.D. degree with the Department of Aeronautical and Aviation Engineering, The Hong Kong Polytechnic University, Hong Kong. His research interests include GNSS and sensor-aided GNSS positioning, SLAM, and multiple sensor fusion in autonomous driving.